Activatable cell penetrating peptides linked to nanoparticles as dual probes for in vivo fluorescence and MR imaging of proteases

Emilia S. Olson[a,b,1], Tao Jiang[a,c,1], Todd A. Aguilera[a,b], Quyen T. Nguyen[d], Lesley G. Ellies[e], Miriam Scadeng[f], and Roger Y. Tsien[a,c,2]

Departments of [a]Pharmacology, [d]Surgery, [e]Pathology, and [f]Radiology, [c]Howard Hughes Medical Institute, and [b]Medical Scientist Training Program, University of California at San Diego, La Jolla, CA 92093-0647

Edited* by Robert Langer, Massachusetts Institute of Technology, Cambridge, MA, and approved December 24, 2009 (received for review September 9, 2009)

High-resolution imaging of molecules intrinsically involved in malignancy and metastasis would be of great value for clinical detection and staging of tumors. We now report in vivo visualization of matrix metalloproteinase activities by MRI and fluorescence of dendrimeric nanoparticles coated with activatable cell penetrating peptides (ACPPs), labeled with Cy5, gadolinium, or both. Uptake of such nanoparticles in tumors is 4- to 15-fold higher than for unconjugated ACPPs. With fluorescent molecules, we are able to detect residual tumor and metastases as small as 200 μm, which can be resected under fluorescence guidance and analyzed histopathologically with fluorescence microscopy. We show that uptake via this mechanism is comparable to that of other near infrared protease sensors, with the added advantage that the approach is translatable to MRI. Once activated, the Gd-labeled nanoparticles deposit high levels (30–50 μM) of Gd in tumor parenchyma with even higher amounts deposited in regions of infiltrative tumor, resulting in useful T_1 contrast lasting several days after injection. These results should improve MRI-guided clinical staging, presurgical planning, and intraoperative fluorescence-guided surgery. The approach may be generalizable to deliver radiation-sensitizing and chemotherapeutic agents.

Molecular navigation | dendrimeric nanoparticles | molecular amplification | targeted imaging agent | transgenic tumor model

Clinical cancer staging currently depends mainly on anatomical imaging with x-ray computed tomography (CT) and MRI. Some tumors can be imaged by PET of glucose uptake, but modest spatial resolution, high cost, exposure to radiation, and imperfect correlation of glucose uptake with malignancy limit the usefulness of PET and its more recent combination with CT. MRI is a particularly attractive imaging modality due to its moderate cost, relatively widespread availability, high spatial resolution tomography, excellent anatomical detail, and lack of radioactivity. Most clinical MRI is either T_1- or T_2-weighted, for which the standard contrast agents are, respectively, gadolinium (Gd) chelates and superparamagnetic iron oxide particles. The difficulty in using MRI for molecular imaging of specific biomolecules rather than for anatomy is sensitivity, because the detection limit is on the order of 10^{-5} M Gd chelate or Fe, respectively (1, 2). Therefore several orders of magnitude of molecular amplification are necessary to detect tumor markers at low nanomolar abundance. T_2-weighted MRI has the additional disadvantages that contrast is usually negative and the iron oxide particles are largely confined to the intravascular and reticuloendothelial compartments. Recently, there has been interest in designing T_1 magnetic resonance (MR) contrast agents that give information beyond that of a standard blood pool agent and detect tumor neovascularization (3, 4), folate receptor (5), and various antigens (6–8). Recent attempts at in vivo MRI of matrix metalloproteinase (MMP) activity have been based on MMP substrates with Gd-DOTA and a hydrophobic chain attached at the N terminus and a PEG chain attached to the C terminus (9). Cleavage of the peptide separates the Gd-DOTA from the hydrophilic PEG and decreases the solubility of the portion containing the Gd-DOTA. The most recent results from this approach show small but significant increases (approximately 0.015 s^{-1}) in proton relaxation rate due to MMP-2 activity (10), but larger and more robust contrast enhancements of invasive MMP-producing tumor would be desirable.

In a separate approach, several groups have begun designing and testing enhanced permeability and retention (EPR)-based dual labeled probes based on either polyamidoamine (PAMAM) dendrimers injected externally for lymph node detection (11) or dual-labeled CLIO particles for tumor detection (12). These molecules do not have targeting beyond that of a blood pool agent. Delayed T_1 MR image enhancement detecting an intratumoral target molecule remains a major challenge, which we seek to address.

In this work, we have modified activatable cell penetrating peptides (ACPPs), molecules previously described by our laboratory for in vivo fluorescence localization of active MMP-2 and -9 in xenograft and transgenic tumor models (13–15). ACPPs are short polycations attached via protease-cleavable linkers to neutralizing polyanions. The polyanion masks the adhesiveness of the polycation until a protease cuts the linker, releasing the polycation and associated cargo to adhere to and be taken up into cells in the immediate vicinity of the protease (Fig. 1*A*). MMP-2 and -9 are proteases whose activity is intimately involved in the process of tumor invasion and metastasis in a wide range of tumor cell lines and clinical examples; see *SI Text* for references. ACPPs containing PLGLAG as linker are predominantly sensitive to MMP-2 and MMP-9 in vivo (15). Previous ACPPs have only been Cy5-labeled, because these are relatively easy to synthesize, and Cy5 fluorescence is readily detectable at the low concentrations (<150 nM) most easily deposited by previously reported ACPPs. The addition of a large molecular weight carrier to the polyglutamate side of the ACPP improved contrast between the tumor and adjacent tissues (15), both by lowering uptake into the latter and by increasing the absolute amount of contrast agent deposited in the tumor.

Author contributions: E.S.O., T.J., and R.Y.T. designed research; E.S.O., T.J., T.A.A., and M.S. performed research; T.J. and L.G.E. contributed new reagents/analytic tools; E.S.O., Q.T.N., M.S., and R.Y.T. analyzed data; and E.S.O., T.A.A., Q.T.N., and R.Y.T. wrote the paper.

Conflict of interest statement: E.S.O.,T.J., T.A.A., Q.T.N., and R.Y.T. have signed scientific advisor agreements with a company founded to develop the technology described in this manuscript.

*This Direct Submission article had a prearranged editor.

Freely available online through the PNAS open access option.

[1]E.S.O. and T.J. contributed equally to this work.

[2]To whom correspondence should be addressed. E-mail: rtsien@ucsd.edu.

This article contains supporting information online at www.pnas.org/cgi/content/full/0910283107/DCSupplemental.

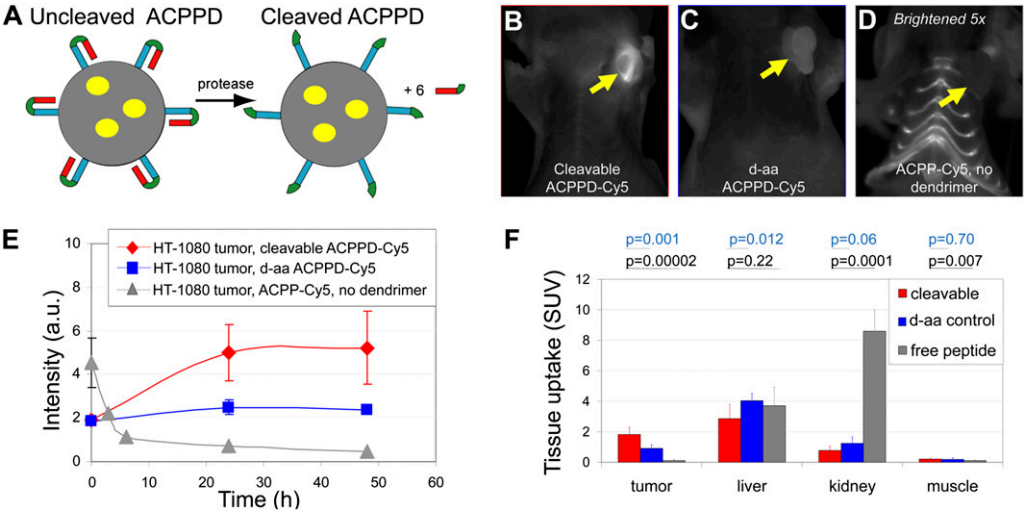

Fig. 1. Cy5-labeled ACPPD cause localized uptake in tumors lasting at least 48 h. (*A*) ACPPD schematic. Each ACPPD consists of a dendrimer (gray circle) covalently attached to the polycationic segments (blue) of several ACPPs (typically about six). In tumors, proteases such as MMP-2 and -9 cleave the linkers (green), releasing polyanions (red) and leaving a highly cationic molecule to stick to and enter cells. Yellow ovals indicate payloads, which can be Cy5 (ACPPD-Cy5) or Gd-DOTA (ACPPD-Gd) or both (dual ACPPD). (*B–D*) Representative fluorescence images (skin removed) 48 h after injection with ACPPD-Cy5 or ACPP-Cy5, each containing 10 nmol of Cy5. Yellow arrows point to tumors. *D* has been brightened fivefold relative to *B* and *C* to make the dim signal from free ACPP-Cy5 visible. For corresponding images before skin removal, see Fig. S2. (*E*) Time courses of tumor fluorescence, viewed through intact skin, from animals injected with cleavable (3 nmol Cy5, $n = 2$, red diamonds) and all-D-amino acid (3 nmol Cy5, $n = 2$, blue squares) ACPPD-Cy5 and an animal injected with cleavable ACPP-Cy5 (10 nmol Cy5, gray diamonds). (*F*) Standardized uptake values in solubilized samples of tumor, liver, kidney, and muscle, 48 h after ACPPD-Cy5 injection ($n = 8$ for cleavable, $n = 5$ for D-amino acid control) and 6 h after ACPP-Cy5 injection ($n = 5$). Pairwise *P* values are shown for each organ type.

Nevertheless, attempts to use this strategy for MRI in tumors have been largely unsuccessful (Fig. S1).

To overcome these obstacles, we have moved the site of macromolecular attachment to the opposite end of the ACPP, i.e., the polycationic domain. Now the macromolecule becomes part of the cargo, so that multiple contrast agents can be attached to it. This configuration retains the previous advantages of macromolecular attachment (i.e., longer tumor circulation time, decreased glomerular and synovial filtration leading to less background uptake) provides some additional amplification (more than one contrast agent per peptide), and facilitates synthesis of multimodality probes. We chose a PAMAM dendrimer as the core macromolecule because such polymers are monodisperse and display multiple amino groups on their spherical surface for derivatization. A fifth generation dendrimer (MW = 28,826, diameter = 5.4 nm) should provide enough molecular weight after derivatization to prevent glomerular filtration yet not too much to hinder intratumoral diffusion.

Results

In our first tests of ACPP-conjugated dendrimers (ACPPDs), two Cy5 labeled constructs were synthesized, tested for purity using HPLC and fluorescence gel electrophoresis, and injected into nude mice bearing HT-1080 xenografts, which express MMP-2 and -9 (13, 15 16). The first was a dendrimer linked to six cleavable ACPPs via maleimides at the C-terminii of the peptides (ACPPD-Cy5) (Fig. 1*A*). The second was a cleavage-resistant control, in which all L-amino acids were converted to D-isomers. Both were labeled with about 3 Cy5′s per dendrimer and finally capped with PEG groups to block all primary amine groups. Initial imaging was with fluorescence to allow histological verification of microscopic localization and comparison with previous configurations. Compared to free ACPPs, the cleavable ACPPD-Cy5 showed greatly diminished skin and joint fluorescence and much higher tumor to thorax ratios, up to 6:1 (Fig. 1 *B–D* and Fig. S2). Furthermore, the fluorescence remained for as long as 48 h, whereas by that time most of the free ACPP had washed out (Fig. 1*E*). The plasma half-life for the molecules was approximately 9 h, compared to less than 10 min for free ACPPs. The cleavable construct was retained in tumor twice as well as its relatively uncleavable D-amino acid control [standardized uptake values (SUVs) were 1.8 ± 0.5, mean± SD, $n = 8$ for the cleavable peptide vs. 0.9 ± 0.2, $n = 5$ for the D-amino acid control, $P = 0.001$] (Table S1), showing that active protease-dependent accumulation makes a significant contribution beyond passive enhanced permeability and retention. In contrast, tumor SUV was only 0.12 ± 0.07 ($n = 5$, $P = 0.00002$) for the cleavable free peptide without dendrimer, Suc-e_8-(Aop)PLGC(Me)AG-r_9-c(Cy5), at the time of best contrast, 6 h after injection (Fig. 1*F* and Table S1). Thus the absolute SUV for the ACPPD-Cy5 was 15-fold higher than for the above ACPP and at least fourfold higher than the best SUV seen with the previous ACPP with PLGLAG linker but lacking macromolecular attachment (14, 15).

We next tested ACPPD-Cy5 in the PyMT breast cancer model. Good contrast was observed (Fig. 2 *A* and *B*), consistent with the known activity of MMP-2 in tumor stroma (15, 17, 18). ACPPD-Cy5 could detect tiny regions of residual tumor attached to pectoralis muscle left after tumor debulking (Fig. 2 *C–E*). As seen previously with ACPPs (15), fluorescence was yet more intense at the stromal interface between tumor and muscle than in the tumor core. Lung metastases were also clearly visible in dissected lung, both grossly and microscopically (Fig. 2 *F–H*), with fluorescence accumulation both in the interior of the metastasis as well as surrounding phagocytes. ACPPDs also highlighted reactive tumor-draining lymph nodes, in which sinusoidal macrophages were particularly bright (Fig. 2*I* and Fig. S3). Finally, as in the previous xenograft model, SUVs were significantly higher (1.5 ± 0.3, $n = 6$) for the cleavable probe than for the D-amino acid control (0.9 ± 0.2, $n = 4$, $P = 0.009$; Fig. S4). A single MMTV-PyMT animal homozygous null for both MMP-2 and MMP-9 was available to be tested with the cleavable probe and gave a similarly low tumor SUV of 0.9.

We next compared ACPPD-Cy5 to other previously published and commercially available near infrared fluorescence probes (Fig. 3*A*). The best known in vivo fluorescence probes for protease activities are polymers heavily labeled with fluorophores that

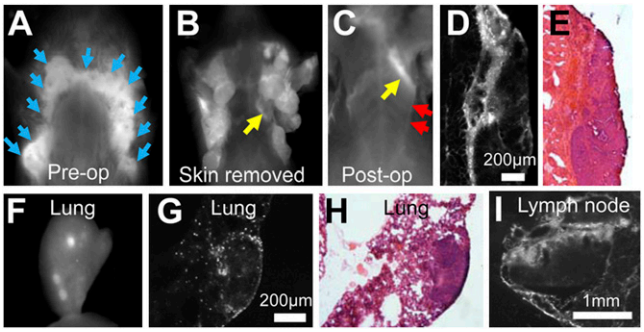

Fig. 2. ACPPD-Cy5 highlights primary and residual tumors in MMTV-PyMT mice. (*A* and *B*) Fluorescence of PyMT mouse 48 h after injection of cleavable ACPPD-Cy5, before (*A*) and after (*B*) skin removal. Tumors are present in all of the mammary fat pads as indicated by blue arrows. (*C*) Image of the same mouse after gross removal of tumor. A strip of protease activity corresponding to tumor (yellow arrows in *B* and *C*) remains attached to the pectoralis muscle (red arrows). (*D* and *E*) Fluorescence (*D*) and hematoxylin/eosin-stained (*E*) frozen section histology confirm the identity of the residual tumor, in this case no larger than 400 μm across (*F*) Gross image of removed lung containing metastases. (*G* and *H*) Fluorescence (*G*) and hematoxylin/eosin (*H*) images showing ACPPD-Cy5 uptake at the edges of a single lung metastasis. (*I*) Fluorescence image of a tumor-draining lymph node. Each fluorescence image is individually scaled to max intensity.

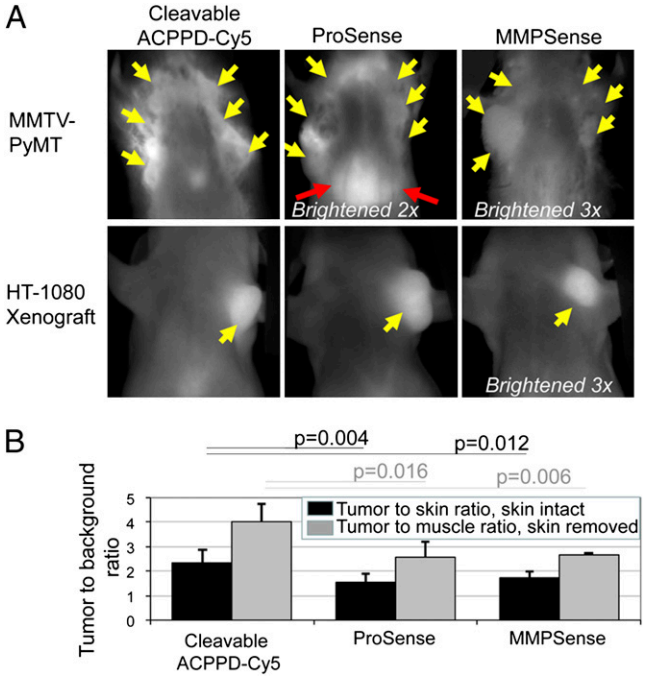

Fig. 3. ACPPD-Cy5 gives equal or better tumor to background contrast than existing dequenching probes. (*A*) Fluorescence images through intact skin of MMTV-PyMT transgenic and HT-1080 xenografted mice 48 h after injection with 1 nmol cleavable ACPPD-Cy5 or 24 h after injection with 2 nmol ProSense or MMPSense. Yellow arrows point to tumor and red arrows indicate liver. Dim images have been brightened by the factors indicated, to enable comparisons. (*B*) Tumor to background ratios for ACPPD-Cy5 and ProSense in the MMTV-PyMT model. Black bars show ratios with skin attached, and gray bars show ratios after skin removal. *P* values for MMPSense and ProSense relative to ACPPD-Cy5s are shown.

quench each other until separated by enzymatic cleavage (16, 19). Such probes for cathepsin and for MMPs are commercially available as ProSense 680 and MMPSense 680, respectively. ACPPD-Cy5's gave better tumor to muscle ratios in vivo (2.4 ± 0.5, $n = 9$) than ProSense (1.6 ± 0.3, $n = 5$, $P = 0.004$) and MMPSense (1.7 ± 0.3, $n = 4$, $P = 0.016$) in the PyMT model (Fig. 3 *A* and *B*). ProSense also gave a particularly large signal over liver, whereas MMPSense was dim overall. Once the skin was removed to reduce scattering and autofluorescence, the ratios of tumor to muscle intensities increased for all three probes in primary PyMT tumors (4.0 ± 0.7, $n = 6$ for ACPPDs; 2.6 ± 0.6, $n = 4$, $P = 0.01$ for Prosense; 2.6 ± 0.1, $n = 3$, $P = 0.006$ for MMPSense) (Fig. 3*B*). ProSense and MMPSense performed better in HT-1080 xenografts (Fig. 3*A*), in which their contrast was not significantly different from our ACPPDs (Fig. S5). Although tumor to background ratios are dependent on tumor size and geometry, these results indicate that ACPPD-Cy5 offers equivalent or better contrast than previously published probes for protease activity that are limited to fluorescence readout.

We next moved toward MRI. A major advantage of dendrimeric nanoparticles is their ability to carry multiple payload molecules. We labeled each dendrimer with 15–30 Gd-DOTA moieties, attached via an amide linkage from one of the DOTA carboxyls to a surface amine of the dendrimer (see *SI Text* for details of preparation; these Gd labeled dendrimers will be referred to as ACPPD-Gd). Such macrocyclic tricarboxylate/monoamide ligands are known to have sufficient in vivo stability to prevent release or toxicity of free Gd^{3+} (20, 21). In vitro relaxivity was approximately 3.7 $(mM\ Gd)^{-1}s^{-1}$ at 7 T. This modest value is due to the steep fall-off of Gd relaxivity at the high magnetic field strengths (7 T) needed for high-resolution imaging in small animals (21, 22). In this set of experiments, 20 nmol ACPPD-Gd, containing 120 nmol ACPP, were injected into the tail vein 48 h before imaging. Several reference samples (phantoms) with different concentrations of Gd-DTPA were placed next to the mouse to account for interscan variation; for quantification, intensities were normalized to a water phantom. In general, Gd accumulation in tissue should increase the longitudinal relaxation rate (R_1) of water protons and increase MR intensity, but to quantify Gd accumulations independent of MR scanning parameters, Gd contents of tissues were also measured postmortem by inductively coupled plasma mass spectroscopy (ICP-MS). At 48 h after injection, R_1 for the tumor had increased by 32% from 0.66 to 0.87 s^{-1}, with the intensity rising by 21% (Fig. 4 *A* and *B*). The approximately 0.2 s^{-1} increase in R_1 and 3.7 $s^{-1}(mM\ Gd)^{-1}$ relaxivity are reasonably consistent with independent measurements by ICP-MS of 30–40 μM Gd in tumor, an SUV of 2.2 ± 0.4, $n = 5$ (Fig. 4*C* and Table S1). In contrast, injection of the D-amino acid negative control increased tumor R_1 and intensity only by 8% and 11%, respectively. The corresponding SUV for Gd was also significantly lower (1.2 ± 0.2, $n = 3$ for D-amino acid control, $P = 0.002$) relative to cleavable ACPPD-Gd. The quantitative agreement of statistically significant increases in relaxation rate and signal intensity with the deposition of Gd confirmed that tumors are accumulating ACPPD-Gd by a substantially protease-dependent mechanism. A similar construct with PLGLAG as a targeting sequence, 6 ACPPs, and 60 Gd-DOTA/dendrimer gave qualitatively similar results. MRI contrast in the tumor persisted for 2–3 days but returned to baseline by 7 days, presumably reflecting eventual washout and excretion of the dendrimeric cargo (Fig. S6). Both the cleavable ACPPD-Gd and D-amino control deposited substantial quantities of Gd into liver, as measured by ICP-MS (Table S1), consistent with the general ability of liver to cleave ACPPs and even their D-amino acid controls (13–15). However, surprisingly little MRI intensity increase was observed in liver (Fig. S6).

One notable feature of the MR images from animals injected with cleavable probe was the presence of bright edges surrounding the tumors, sometimes tunneling into neighboring parenchyma. To determine whether these bright edges seen on MRI represented regions of infiltrative tumor that could potentially be removed under fluorescence guidance, a dual labeled probe with both Gd

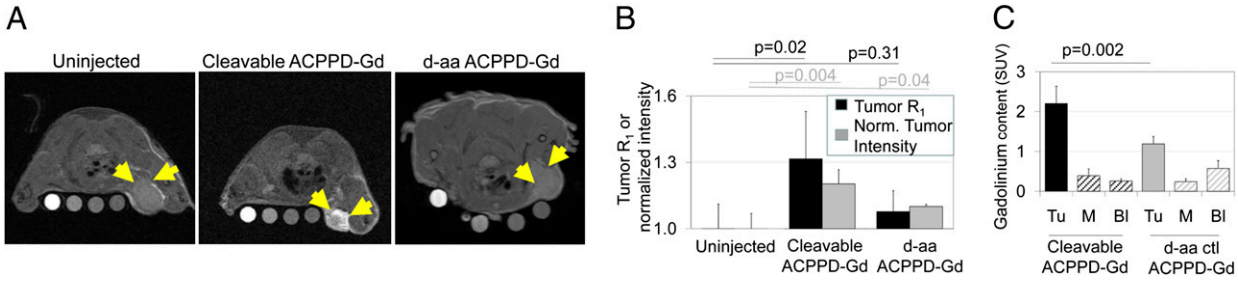

Fig. 4. Gd-labeled ACPPD's allow visualization of protease activity by T_1-weighted MRI. (*A*) MR axial slices of animals bearing HT-1080 xenografts before injection or 48 h after injection of cleavable ACPPD-Gd or an all-D-amino acid control as indicated. Yellow arrows point to tumors. Each image includes phantoms containing 250, 50, 10, and 0 μM Gd-DTPA from left to right. (*B*) Tumor intensities (black) and R_1 (gray) for cleavable and D-amino acid control ACPPD-Gd relative to those of uninjected mice. Tumor intensities have been normalized to water phantom intensities on the same image to account for variability between scans. *P* values are given for R_1 and normalized intensity relative to uninjected control animals. (*C*) Standardized uptake values at 48 h for Gd (quantitated using ICPMS) in tissues from animals injected with either the cleavable ACPPD-Gd or D-amino acid control. Tu = tumor, M = muscle, Bl = blood.

and Cy5 ("dual" ACPPD) was synthesized and injected into transgenic PyMT mice (Fig. 5 *A-E*), or animals bearing MDA-MB-435 (23) or HT-1080 tumors. The HT-1080 cells had been injected either s.c., typically generating a well encapsulated tumor, or intramuscularly, because this empirically increased the likelihood that the tumor cells would infiltrate into surrounding normal tissue (Fig. 5 *F–L* and Fig. S7). The dual ACPPD made tumors visible by both MR and fluorescence (Fig. 5 *A* and *B*). Tumors were then resected and postoperative MR and fluorescence images examined for residual tumor (Fig. 5 *C* and *D*). Where residual regions of hyperintensity were noted, the tumor margin was excised further and analyzed using hematoxylin/eosin staining to confirm the presence of tumor (n = 3, Fig. 5*E*). In addition to diffuse parenchymal uptake of dual ACPPD, HT-1080 tumors injected intramuscularly showed additional enhancement at the tumor edges (Fig. 5*F*). Frozen section histology done on excised margins showed that the brightest fluorescence came from tumor infiltrating chronically inflamed surrounding muscle (Fig. 5 *G–H*) containing many macrophages (Fig. S8). To verify increased MMP activation, in situ zymography and hematoxylin/eosin staining were done on the same section (Fig. 5 *I–L*). The overlay demonstrates that the most intense ACPPD uptake correlates with high MMP activity at the invasive edge of tumors. Such highlighting of invasive margins may be useful intraoperatively and to evaluate the stage and aggressiveness of tumors.

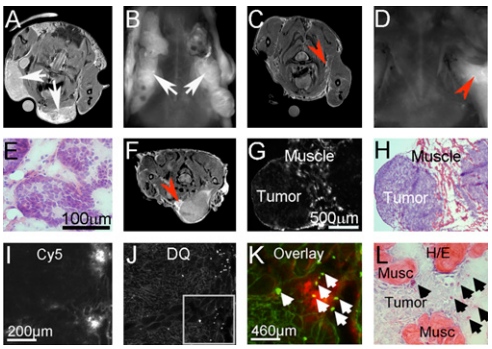

Fig. 5. Regions of especially bright Gd and Cy5 labeled dual-ACPPD uptake on MRI correspond to regions of active MMP's, infiltrative tumor and associated inflammation on histology. (*A*) Axial MR and (*B*) fluorescence (skin off) images of a transgenic PyMT mouse with high tumor burden (white arrows) (*C*) Axial MR and (*D*) fluorescence images of the same mouse after surgical removal of tumor under white light. Red arrows point to regions of residual hyperintensity on MR and fluorescence imaging. Gamma has been adjusted for image clarity. (*E*) Regions of hyperintensity on MRI were resected using fluorescence imaging and stained with hematoxylin/eosin to verify the presence of tumor. (*F-H*) Residual tumor collected under similar conditions from a nude mouse bearing an HT-1080 xenograft (*F*). The red arrow points to an area of infiltrative tumor that was largely missed at the time of surgery. The residual tissue was removed and analyzed further. (*G*) Fluorescence image of a section showing intense dual ACPPD uptake in inflammation surrounding the infiltrative edge of tumor (*H*). (*I–L*) Fluorescence histology confirming that the hyperintense region of ACPPD uptake corresponds to the presence of MMP activity and infiltrative tumor. (*I*) Fluorescence imaging of dual-ACPPD uptake and (*J*) DQ-gelatin on the same slice verified the presence of scattered protease producing cells. (*K*) Boxed region from *I* and *J*, overlaid to show rough colocalization of Cy5 (red) and DQ-positive regions (green). (*L*) Same section restained with hematoxylin/eosin to verify tissue identity. Purple hematoxylin has been image-enhanced for clarity.

Discussion

ACPPDs have many advantages over other optical and MR-based probes. First, their amenability to dual labeling for MR and fluorescence provides ideal correlation between tomographic imaging that can detect tumors anywhere in the body, with higher-resolution but more superficial imaging ideal for intraoperative surgical guidance (23). Previous fluorescent probes for enzyme activities either rely on fluorescence-specific mechanisms such as dequenching (16, 19) or lack amplification (24). Second, ACPPDs are activated by proteases that are upregulated by a wide variety of tumors from differing anatomical sites, making them more applicable as potential diagnostic agents than molecules that target a particular antigen only upregulated in a subset of cancers. Their retention in regions of protease activity allows them to highlight small but invasive tumors and metastases that might not otherwise be noted on routine radiological examination. This added information may be particularly useful in the staging of certain cancers, in which tumor infiltration of a capsule plays a critical role in prognosis. Third, their increased molecular size reduces the high background uptake previously seen for unadorned ACPP's and allows for additional tumor accumulation based on enhanced permeability and retention although still remaining small enough to penetrate into solid tumors. For all of these reasons, ACPPDs may be useful for clinical purposes beyond the academic exercise of detecting MMP activity in mouse models of cancer.

The combined mechanisms give tumor uptake of up to 50 μM Gd so far, enough for visualization using T_1 weighted MRI and resulting in far greater and longer-lasting relaxation rate increases than any previously reported for MMP-sensitive probes (9, 10). A significant component of the ACPPD uptake was cleavage dependent, in contrast to recent results (25) with a superficially similar mechanism of protease dependent "unveiling", in which six arginine-rich cell penetrating peptides (CPPs) attached to each 85-nm nanoparticle were sterically "veiled" by about sixty 10 kDa

PEG chains also attached to each nanoparticle but via MMP-2 cleavable peptides. Attack by MMP-2 released the PEG chains, revealing the CPPs. However, uptake into the tumor was the same whether the peptides were cleavable L-amino acids or cleavage-resistant D-amino acids (25), so tumor contrast proved to be entirely due to passive mechanisms such as enhanced permeability and retention. Our dendrimers are much smaller (hydrodynamic diameter approximately 9 nm), which is possible because each CPP is masked by a single electrostatically neutralizing polyglutamate (<1.2 kDa) rather than ten sterically shielding 10 kDa PEGs. The smaller nanoparticle size should facilitate diffusion both deeper into the tumor and back into the circulation until the linkers are proteolyzed. Therefore protease cleavage can and does enhance net tumor retention of these smaller nanoparticles. The dependence of adhesiveness on the number of cleavage events has not been quantified for either mechanism, but complete unmasking requires one cleavage per ACPP vs. about 10 cleavages per PEG-veiled CPP.

Two major problems with our original unadorned ACPPs were high background, particularly in cartilage and kidney (15) and significant mortality in mice injected with 75 and 150 nmol per 30 g animal (14). Now that the ACPPs have been conjugated through their polycationic C-terminii to dendrimers, the contrast between tumor and background tissues including cartilage and kidney has improved greatly and is comparable to or somewhat better than ACPPs conjugated via their polyanionic N-terminii to similar macromolecules (15). Figs. 2 and 5 show that small metastases, tumor associated lymph nodes, residual tumor (200 μm), and associated inflammatory microenvironment are labeled by the fluorescence probes and are easily distinguished from background. This attachment mode, where the dendrimer is retained rather than discarded after protease attack, gives much higher SUVs and the flexibility to load multiple copies of Gd chelate, fluorescent dye, and potentially other payloads, making possible ACPPD-based MRI as well as dual modality imaging. No deaths or apparent toxicity were seen even after repeated anesthetization and injection with up to 20 nmol dendrimer carrying a total of 120 nmol ACPP. This improvement suggests that our current method for attachment of ACPPs to macromolecular carriers may help selective delivery of chemotherapeutic cargoes to tumors. Meanwhile, the dual label already promises synergistic benefits for fluorescence-guided surgery by allowing early whole-body scanning for tumors, providing tomographic biochemical landmarks on the MR images for surgical planning, real-time submillimeter intraoperative guidance by fluorescence, and postoperative evaluation of the completeness of resection (23).

Materials and Methods

Synthesis. Peptides Suc-e_8-(Aop)-PLGC(Me)AG-r_9-c-NH_2 and Suc-e_8-(Aop)-plgc(Me)ag-r_9-c-NH_2 were synthesized by standard Fmoc chemistry and attached to the PAMAM dendrimer via the C-terminal cysteine and a maleimide linker. Lowercase letters indicate D-amino acids. Aop means 5-amino-3-oxapentanoyl, a flexible hydrophilic linker to facilitate hairpin conformation. C(Me) indicates (S-methyl)cysteine, which is a particularly favorable amino acid at the S_1' position (26). For synthetic details, see *SI Text*. In brief, after attachment of the peptide, approximately three Cy5 molecules or 15–30 DOTA were attached to the dendrimer via an amide linkage. Finally, the remaining amino groups were capped with methoxyPEG4. For constructs with no Cy5, chelation of Gd was done in glycine buffer (pH 6) at 80 °C for 3 h. For dually-labeled ACPPDs, Gd incorporation without heating was necessary (ammonium acetate buffer, pH 6 overnight). In all three cases, purification was done by centrifugation through a membrane with a 10-kD molecular weight cut-off (Amicon). For Cy5 labeled constructs, concentration of the dendrimer was assessed by total weight of the compound. The number of Cy5′s per dendrimer was assessed by comparing the concentration of dendrimer to the absorbance of Cy5. For Gd labeled constructs, the concentration of dendrimer was assessed by weight and the concentration of Gd was assessed by inductively coupled plasma mass spectroscopy (Bodycote Analytical), both immediately post synthesis and at the time of injection. Wherever possible, purity of the fluorescent species was independently assessed by tricine gel electrophoresis and was typically found to be over 95%.

Animals. Nude mice harboring HT-1080 tumors (3-8 mm) were obtained from Explora Biosciences. MMTV-PyMT mice and associated knockouts were bred at University of California at San Diego. Genotype was verified by PCR analysis. All animal procedures were approved by University of California at San Diego's institutional animal care and use committee.

Optical Imaging. Animals were anesthetized with 80 mg/kg ketamine and 40 mg/kg midazolam. One to three nanomoles (nmol) of each probe was injected intravenously, as specified by the manufacturer. For ProSense 680 and MMPSense 680, 2 nmol of probe was injected as specified by the manufacturer (VisEn Medical). Animals were imaged for 1 and 3 s exposures using a Maestro spectral deconvolution imager (700 nm) using a 640/48 excitation filter (CRI) for up to 1 h following the original injection. Following imaging, animals were returned to their cages and warmed using delta phase pads. At 6 h, 24 h, and 48 h, animals were reanesthetized and imaged. "Tumor to background" contrast ratios were taken by taking a region over the tumor and a region over the thorax in Adobe Photoshop. After 48 h, animals were killed, organs harvested, and tissues frozen. For ProSense 680 and MMPSense 680, animals were sacrificed after 24 h as per the manufacturer's instructions.

Optical SUVs. Frozen tissues were defrosted and a representative 30-mg sample cut in the absence of fluorescence guidance. For some tumors known to be heterogeneous such as the PyMT tumors, two to three such 30-mg samples were processed separately and averaged. Each 30-mg slice of tissue was then added to 100 μL SDS lysis buffer (1% SDS, 20 mM Tris buffer, pH 7.6), ground using a disposable pestle and heated to 80 °C for 10 min. To ensure cell lysis, samples were then microwaved twice for 4 s. To ensure equal treatment of samples, tubes were centrifuged for 10 min, frozen and imaged using the Maestro. Integrated intensities were calculated using Image J. Due to minor variations in the number of Cy5 labels per dendrimer, two tissue specific point calibrations were done for each conjugate separately. These standards were prepared by cutting approximately 30-mg samples from tumor, liver, kidney, and muscle from uninjected animals, spiking them with 100 nM final concentration of the injected peptide and processing them as before. Based on concentration curves from one of the conjugates, linearity of signal with concentration was assumed. SUVs are defined as (nmol Cy5/weight of tissue sample)/(total nmol injected/total weight animal).

Fluorescence Histology. Sections were cut at 20 μm for HT1080 and PyMT tumors and 25 μm for PyMT metastases then examined using a Zeiss Lumar dissecting microscope (exposure times 5–15 s, ex 620/60, em 700/75). For in situ zymography, DQ gelatin was obtained from EMD and processed as per the manufacturer's instructions. Serial sections were stained using a standard hematoxylin and eosin procedure. Images shown in text were background subtracted based on the lowest pixel value.

MRI. Animals were anesthetized and injected as described for optical imaging. At 48 h, animals were taken to University of California at San Diego's 7T magnet, anesthetized using isoflurane (3% loading dose, 1% maintenance dose), and imaged using a T1-weighted RARE (Tr = 2595 ms, Te = 7.5 ms, NEX = 10, slice thickness 0.3 mm, acquisition matrix 256 × 256), a T1-weighted MSME (Tr = 498 ms, Te = 8 ms, 10 NEX, slice thickness 0.3 mm, acquisition matrix 128 × 256), and a Tru-FISP (single slice, slice thickness 0.5 mm, Tr = 3, Te = 1.5 ms, 4 NEX, acquisition matrix 128 × 128) to obtain T1s (27). MRI data were processed using either Paravision (Brucker) or Amira 4.1.1 (Mercury). Every effort was made to exclude regions of gross necrosis in the middle of tumors. Images shown in text were windowed for ease of visibility after image processing was complete. Tumor was identified in vivo using T1 and T2 images, and its identity confirmed at dissection using fluorescence histology if warranted.

Gd SUVs. Following the 48-h imaging session, animals were sacrificed and tissues removed and frozen. They were defrosted, weighed, dissolved in nitric acid, and sent to Bodycote Analytical Services for quantitative Gd analysis using ICP-MS. Two microliters of the injectate was processed similarly and analyzed in parallel. SUV are defined as (nmol Gd/weight tissue)/(total nmol injected/total weight animal). One tumor specimen was excluded due to excessive central necrosis (>50%).

ACKNOWLEDGMENTS. We thank Jessica Crisp for helpful discussions and Perla Arcaira and Timothy Salazar for help in measuring SUVs. We also thank Dr. Beth Friedman for helpful discussions and help with SI figure preparation. This work was supported by Howard Hughes Medical Institute and Grant W81XWH-05-1-0183 from the Department of Defense Breast Cancer Research Program.

1. Khemtong C, et al. (2009) In vivo off-resonance saturation magnetic resonance imaging of alphavbeta3-targeted superparamagnetic nanoparticles. *Cancer Res* 69: 1651–1658.
2. Mills PH, Ahrens ET (2007) Theoretical MRI contrast model for exogenous T2 agents. *Magn Reson Med* 57:442–447.
3. Ke T, et al. (2007) RGD targeted poly(L-glutamic acid)-cystamine-(Gd-DO3A) conjugate for detecting angiogenesis biomarker $\alpha(_v)$ β_3 integrin with MRT, mapping. *Int J Nanomedicine* 2:191–199.
4. Burtea C, et al. (2008) Molecular imaging of α_v β_3 integrin expression in atherosclerotic plaques with a mimetic of RGD peptide grafted to Gd-DTPA. *Cardiovasc Res* 78:148–157.
5. Konda SD, Wang S, Brechbiel M, Wiener EC (2002) Biodistribution of a 153 Gd-folate dendrimer, generation = 4, in mice with folate-receptor positive and negative ovarian tumor xenografts. *Invest Radiol* 37:199–204.
6. Towner RA, et al. (2008) In vivo detection of c-Met expression in a rat C6 glioma model. *J Cell Mol Med* 12:174–186.
7. Reynolds PR, et al. (2006) Detection of vascular expression of E-selectin in vivo with MR imaging. *Radiology* 241:469–476.
8. Lipinski MJ, et al. (2006) MRI to detect atherosclerosis with gadolinium-containing immunomicelles targeting the macrophage scavenger receptor. *Magn Reson Med* 56: 601–610.
9. Lepage M, et al. (2007) Noninvasive detection of matrix metalloproteinase activity in vivo using a novel magnetic resonance imaging contrast agent with a solubility switch. *Mol Imaging* 6:393–403.
10. Lebel R, et al. (2008) Novel solubility-switchable MRI agent allows the noninvasive detection of matrix metalloproteinase-2 activity in vivo in a mouse model. *Magn Reson Med* 60:1056–1065.
11. Koyama Y, et al. (2007) A dendrimer-based nanosized contrast agent dual-labeled for magnetic resonance and optical fluorescence imaging to localize the sentinel lymph node in mice. *J Magn Reson Imaging* 25:866–871.
12. Talanov VS, et al. (2006) Dendrimer-based nanoprobe for dual modality magnetic resonance and fluorescence imaging. *Nano Lett* 6:1459–1463.
13. Jiang T, et al. (2004) Tumor imaging by means of proteolytic activation of cell-penetrating peptides. *Proc Natl Acad Sci USA* 101:17867–17872.
14. Aguilera TA, et al. (2009) Systemic *in vivo* distribution of activatable cell penetrating peptides is superior to cell penetrating peptides. *Integrative Biology* 1:371–381.
15. Olson ES, et al. (2009) *In vivo* characterization of activatable cell penetrating peptides for targeting protease activity in cancer. *Integrative Biology* 1:382–393.
16. Bremer C, Bredow S, Mahmood U, Weissleder R, Tung CH (2001) Optical imaging of matrix metalloproteinase-2 activity in tumors: Feasibility study in a mouse model. *Radiology* 221:523–529.
17. Maglione JE, et al. (2001) Transgenic Polyoma middle-T mice model premalignant mammary disease. *Cancer Res* 61:8298–8305.
18. Pedersen TX, et al. (2005) Extracellular protease mRNAs are predominantly expressed in the stromal areas of microdissected mouse breast carcinomas. *Carcinogenesis* 26: 1233–1240.
19. Bremer C, Tung CH, Bogdanov A, Jr, Weissleder R (2002) Imaging of differential protease expression in breast cancers for detection of aggressive tumor phenotypes. *Radiology* 222:814–818.
20. Harrison A, et al. (1993) Hepato-biliary and renal excretion in mice of charged and neutral gadolinium complexes of cyclic tetra-aza-phosphinic and carboxylic acids. *Magn Reson Imaging* 11:761–770.
21. Jászberényi Z, et al. (2007) Physicochemical and MRI characterization of Gd3+-loaded polyamidoamine and hyperbranched dendrimers. *J Biol Inorg Chem* 12:406–420.
22. Bryant LH, Jr, et al. (1999) Synthesis and relaxometry of high-generation (G = 5, 7, 9, and 10) PAMAM dendrimer-DOTA-gadolinium chelates. *J Magn Reson Imaging* 9: 348–352.
23. Nguyen QT, et al. (2010) Molecular fluorescence imaging guidance during surgery decreases residual cancer and improves survival. *Proc Natl Acad Sci USA*, in press.
24. Veiseh M, et al. (2007) Tumor paint: A chlorotoxin:Cy5.5 bioconjugate for intraoperative visualization of cancer foci. *Cancer Res* 67:6882–6888.
25. Harris TJ, et al. (2008) Protease-triggered unveiling of bioactive nanoparticles. *Small* 4:1307–1312.
26. McGeehan GM, et al. (1994) Characterization of the peptide substrate specificities of interstitial collagenase and 92-kDa gelatinase. Implications for substrate optimization. *J Biol Chem* 269:32814–32820.
27. Schmitt P, et al. (2004) Inversion recovery TrueFISP: Quantification of T(1), T(2), and spin density. *Magn Reson Med* 51:661–667.